
Reconstructing micro-magnetic vector fields based on topological charge distributions via generative neural network systems

Kyra H. M. Klos¹ Jan Disselhoff²
Karin Everschor-Sitte³ Friederike Schmid¹

¹ Institut of Physics, Johannes Gutenberg-University, Mainz

² Institute of Computer Science, Johannes Gutenberg-University, Mainz

³ Faculty of Physics & Center for Nanointegration Duisburg-Essen,
University of Duisburg-Essen, Duisburg

kyklos@uni-mainz.de jadissel@uni-mainz.de

Abstract

Topological defects are omnipresent in physical and biological systems. These localized deforming structures have an intrinsic multiscale nature: Their microscopic structure can be represented macroscopically as interacting particles. In this work, we extend a Wasserstein Generative Adversarial Network (WGAN) by incorporating physical constraints, to reconstruct realistic microscopic structures from macroscopic topological defect distributions and other physical inputs. Using the two-dimensional XY-model as proof of concept, our method generates physical realistic micro-magnetic vector configurations verified through multiple measures. This approach enables efficient dynamical simulations of large defect systems while providing robust support for the analytical interpretation of experimental data. By leveraging our network, microscale information can be accurately recovered, bridging the gap between large-scale dynamics and fine-grained structural details.

1 Introduction

Various physical systems and material properties are profoundly influenced by localized microscopic structures which inherently emerge due to specific boundary conditions, external fields and temperature fluctuations. These so called topological defects are perturbations of the underlying ordering field that cannot be removed through any continuous transformation, making them topological and usually physically stable [3]. Their intrinsic stability makes topological defects valuable in many different areas of research. Novel applications include data storage, transportation and general alternative methods of computation [12] as well as their use as a control mechanism of bacteria dynamics in medical research [20].

While these defects can effectively be modelled as macroscopic quasi-particles with a non-zero topological charge k , their local interactions on the microscopic scale influence the system globally. The resulting long-range, complex interactions make modelling these structures crucial, but computational limitations for large, detailed simulations and experimental constraints restrict access to such microscopic information. In material science, dynamical models have been developed solely for the purpose of describing the mechanism of macroscopic defect particles. However to calculate the resulting material properties, one needs to be able to reconstruct the underlying microscopic field structure from a

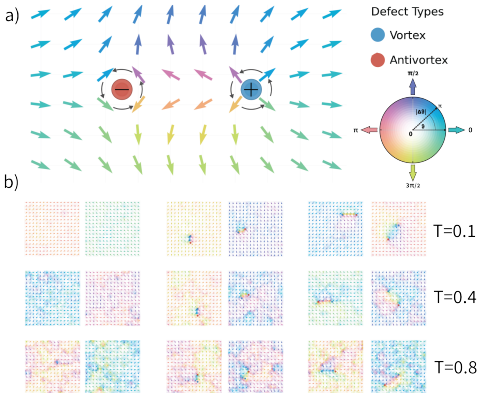


Figure 1: Micro-magnetic vector fields in the two-dimensional XY-model: a) Close up of a defect pair, with the red and blue circles denoting topological charges of $k = -1$ and $k = +1$. b) Examples of our simulated training data.

fect distributions. By leveraging the inherent multiscale nature of these defects, we aim to bridge the gap between macroscopic quasi-particle and microscopic field description, thereby enhancing our understanding of defect behavior and interactions. We do so by using a U-Net architecture, trained as a Generative Adversarial Network (GAN), which enables us to sample from a microscopic field distribution in a single forward pass thereby providing the opportunity for efficient large-scale simulations and experimental data analysis support. We specifically choose to use a U-net generator, as we want our model to connect different length scales and to “enhance” the resolution of the macroscopic description to its underlying microscopic one [8, 21]. To show the validity of our approach, we use the two-dimensional XY-model on a square lattice as a toy model, due to its simultaneous basic description and rich physical implication and interaction pattern. Used to model superfluid helium [3, 16] the XY-Model is a planar model with two-dimensional magnetic ordering and non-linear next neighbor interaction of normed micro-magnetic vectors $S_i(\vartheta_i) = (\cos(\vartheta_i), \sin(\vartheta_i))^T$ with angle ϑ_i , placed on lattice site i . The defects ν in this system, see Figure 1 a), are called vortex and antivortex depending on their topological charge of $k = +1$ and $k = -1$ respectively. Additionally, the system shows temperature-induced long-range fluctuations in wave patterns. Example configurations can be seen in Figure 1 b), showing the temperature-dependent influence of a defect pair on the global magnetic ordering.

2 Methods

In the following, we describe the process of creating a generative network capable of mapping a topological charge distribution back to physically realistic micro-magnetic vector lattices for a given temperature, using an architecture that is as small and computationally efficient as possible.

First, we produce our training data using the Metropolis-Hastings algorithm [7]. Each training example is a $N = L \times L$ sized lattice of two-dimensional micro-magnetic vectors with periodic boundary conditions, modeled by a planar XY-model. For our network experiments, we produce 250,000 data samples for each temperature T using $L = 16$. Note that the emergence of defects is highly improbable in low-temperature settings. To address this, we add an additional constraint to the acceptance step of the Monte Carlo simulation, allowing us to enforce specific defect distributions independent of the temperature T . For the produced micro-magnetic vector fields, we calculate a dual lattice containing the topological charges encoded as $k = \pm 1$ and $k = 0$ for (anti-)vortices and topologically trivial spots, respectively.

Based on this data, the network learns the inverse mapping from charge distribution to micro-magnetic vector lattices. Since this mapping is not unique, even when conditioned on the temperature, we opted to use a conditional Wasserstein Generative Adversarial Network (cWGAN) [14]. This extension of the standard GAN has been shown to exhibit more stable training behavior and avoids the “mode collapse” phenomenon. While training a GAN can

given particle defect distribution.

In this work, we present a multiscale approach for reconstructing realistic microscopic structures of topological defects from macroscopic topological defect distributions and other physical inputs, leveraging the capabilities of a specifically designed generative model. Realizing this reconstruction provides greater insight into defect-driven phenomena, facilitates the analysis of experimental data and enables more accurate and scalable simulations of large defect systems.

In the pursuit of modeling topological defects with deep learning techniques, existing research has primarily focused on detecting defects within simulated and experimental data [1, 24] and generating general mesoscopic ordering field distributions [18]. Our work on the other hand addresses a complementary yet crucial challenge, namely the reconstruction of the physical realistic microscopic field configurations that underlie observable macroscopic topological defects.

be time-consuming, the trained networks are efficient in generating results and produce high-quality outputs, rivaling those of more recent generative models such as diffusion models. [11]. Following the WGAN framework, the critic maps the input lattice vector field and embedded temperature label to a continuous measure of realness, distinguishing real from generated data. To implement this the critic is constructed of convolution layers, LeakyReLU [13] and optional Instance-Norm [23] layers.

The generator, in light of the inherent multi-scale character of topological defects, is based on a U-Net architecture (see Figure 2). This model is split into an encoder and a decoder, with shortcuts connecting them on each depth level. Each encoder block contains a convolution layer, LeakyReLU activation function and subsequent pooling, while the decoder block contains convolution layers, LeakyReLU activation and transposed convolution to up-sample the intermediate results. Since transposed convolution is prone to aliasing effects [17] we also experimented with interpolation layers as a way of upsampling. These layers, however, are unable to infer the discontinuous nature of our vector field and the corresponding underlying topology, completely disrupting the learning process.

In contrast to typical generators, where the noise is provided solely as primary input, we only inject noise at the bottleneck layer, to prevent the network from reintroducing it at lower depths. In our experiments, adding noise at any other position significantly inhibited the learning process. We train these networks using Wasserstein losses combined with an additional Gradient Penalty for the critic, increasing the stability of our training [9]. In addition to the cWGAN loss, the generator training includes the physics-based loss $\tilde{\mathcal{L}}_G$:

$$\tilde{\mathcal{L}}_G := \sum_r^N \alpha_r (k_r - k_r^{real})^2 \quad (1)$$

Here k_r^{real} is the topological charge at defect lattice site r . Since most spaces do not contain a topological charge we use α_r for importance weighting anti-proportional to their respective density, i.e. non-zero charges are weighted with a factor of N , and other positions with a factor of one. To calculate topological charge k_r we need to capture the change in the local vector field surrounding the defect as seen in Figure 1 a). With plaquette \square_r describing the closest surrounding values of k_r in the micro-magnetic lattice, k_r is defined as:

$$k_r = \frac{1}{2\pi} \oint d\vartheta = \frac{1}{2\pi} \sum_{\{i,j\} \in \square_r} \text{saw}(\Delta\vartheta_{ji}), \text{ with } \text{saw}(x) = \begin{cases} x & -\pi < x < +\pi \\ x + \text{sgn}(x)2\pi & |x| \geq \pi \end{cases} \quad (2)$$

where the angle differences $\Delta\vartheta_{ji} = \vartheta_j - \vartheta_i$ between neighboring micro magnetic vector pairs $\{i, j\}$ on lattice sides i, j in the plaquette are calculated counterclockwise. Unfortunately, equation 2 is ill-suited for gradient calculations, as it is either constant or non-continuous at every position. To mitigate this, we approximate the winding number k_r using the cross product of plaquette micro-magnetic vectors S_{ij} in z direction.

$$k_r \approx \frac{1}{4} \sum_{\{i,j\} \in \square_r} S_{ix}S_{jy} - S_{jx}S_{iy} \quad (3)$$

This enables us to include approximated topological charge information into the generator training. For the results discussed in the next section, we are training our networks for 120 epochs in batches of 64 on a 'NVIDIA RTX 3080'. We are using Adam optimizer [10] and a starting learning rate of 10^{-4} for both s. The physical loss is included as a regularizer after 40 epochs with a learning rate of 10^{-5} . We update the critic four times for each generator update step, to ensure valid gradients in the generator. The generator U-Net uses four encoder and decoder blocks with output channels [64,128,256,256] and [256,128,64,2] respectively. All weights are initialized with the standard 'PyTorch' initialization. All models and training code uses 'PyTorch v2.2.2' [19].

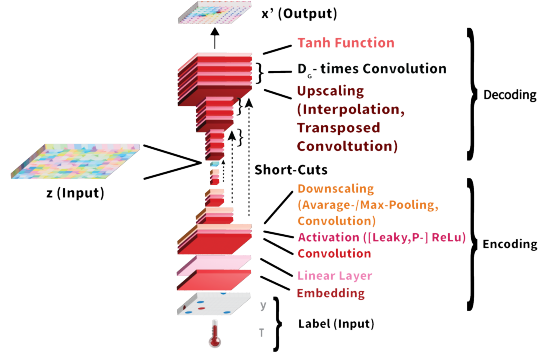


Figure 2: The basic shape of our U-Net-based generator. Topological charge information y as well as temperature T are added from the start, while noise z is only added in the bottleneck of the U-net.

3 Results

In the training process of a WGAN, the loss function of the generator is not a clear indicator of performance. To validate the training progress over time we track two major measurements: The vorticity ν , measuring the topological charge distribution in the generated vector field, and the magnetisation $\langle |M| \rangle$, giving an indication of the overall direction of the field, as seen in Figure 3. In both cases our generator learns to produce more realistic images over time. While the major increase in capability happens in the first few epochs, the network continues to refine its prediction for a long time to a high precision. This is of particular importance for our problem as even small errors can lead to physically unrealistic outputs.

To evaluate the performance of our trained network, we compare our generated fields with simulated baseline data regarding their physical and topological characteristics for singular defect pair configurations in low temperature $T = 0.1$. The physical observables [3, 6] are used as statistical means to compare the consistency of field and defect structure and are shown depending on their distance d_ν in Figure 4 a)-b). Most measures in 4 a) show strong alignment with an accuracy of around $[0.92 - 0.99]$ calculated via R^2 defined in equation 4. The mean strength of individual angle deviations over the full lattice, tracked by energy $\langle E \rangle$, shows an overall match.

However, the specific heat C_v - a descriptor of the energy variance in a defect configuration ensemble - deviates significantly from the ground truth. Since this measure is dependent on the 4th order of the micro-magnetic vectors $\mathcal{O}(S^4)$, even small numerical errors can cause such large discrepancies.

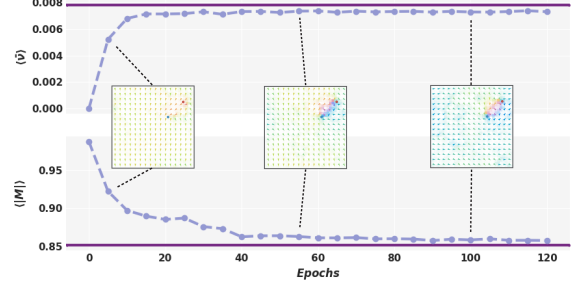


Figure 3: Training process of generator (light violet) shown via the comparison to the simulated baseline (dark violet) of the defect distribution [vorticity ν] and mean alignment of micro-magnetic vectors [magnetisation $\langle |M| \rangle$] for $T = 0.1$.

network, we compare our generated fields with simulated baseline data regarding their physical and topological characteristics for singular defect pair configurations in low temperature $T = 0.1$. The physical observables [3, 6] are used as statistical means to compare the consistency of field and defect structure and are shown depending on their distance d_ν in Figure 4 a)-b). Most measures in 4 a) show strong alignment with an accuracy of around $[0.92 - 0.99]$ calculated via R^2 defined in equation 4. The mean strength of individual angle deviations over the full lattice, tracked by energy $\langle E \rangle$, shows an overall match.

However, the specific heat C_v - a descriptor of the energy variance in a defect configuration ensemble - deviates significantly from the ground truth. Since this measure is dependent on the 4th order of the micro-magnetic vectors $\mathcal{O}(S^4)$, even small numerical errors can cause such large discrepancies.

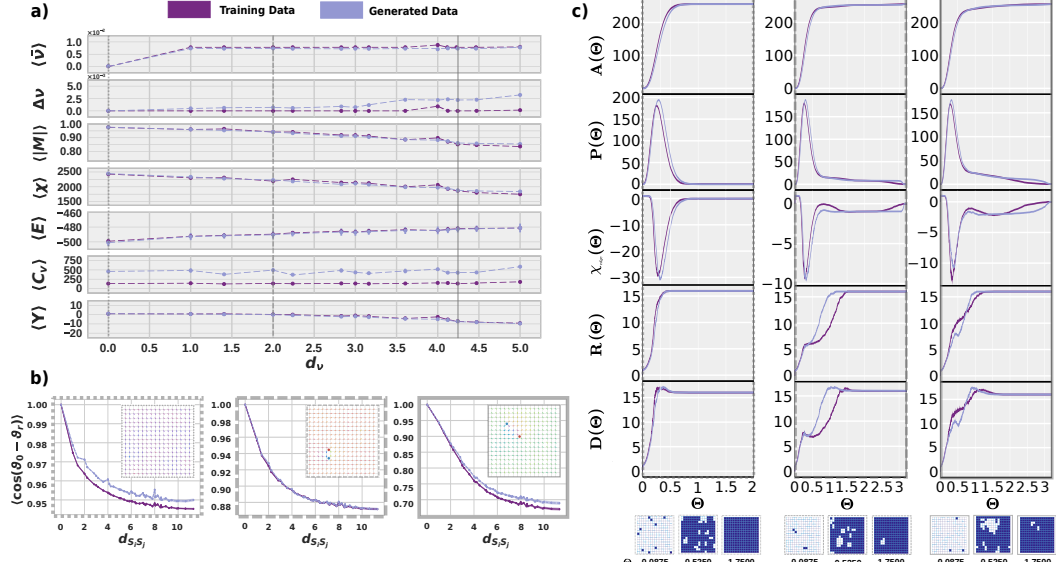


Figure 4: Comparison of measures based on the analysis of simulated (dark violet) and generated (light violet) micro-magnetic vector fields for temperature label $T = 0.1$: a) Mean physical measures depending on defect pair distance d_ν of data of 1000 samples each. b) Global micro-magnetic vector correlation function depending on their distance $d_{s_i s_j}$ for no defects $d_\nu = 0$. (left), close defects $d_\nu = 2$. (middle) and far defects $d_\nu \approx 4.14$ (right), with representative generated examples. c) Topological measures for series of graph representations respectively for a set of 100 sampled micro-magnetic vector fields depending on the filtration parameter Θ , for no (left), close (middle) and far defects (right) with exemplary graph representations of the vector fields in b).

In future works we aim to increase the strength of both generator and critic to capture these higher modes. Overall this indicates that the generated micro-magnetic vector fields can - to an extent - reproduce physically realistic thermal mean behavior. Generated examples can be found in Figure 4 and 5 b). We are also able to reconstruct the underlying global correlation $\langle S_i S_j \rangle$ of the micro-magnetic vectors $S_{i,j}$ with $i, j \in N$ with a mean accuracy of [0.70] calculated via 4 as seen in Figure 4 b), demonstrating mostly realistic long range interaction patterns in the generated data. In order to globally quantify the topological features of individual vector fields we additionally employ topological data analysis [4]. We do so by building a series of graph representations for each individual vector field lattice based on the mechanisms of persistence homology [22, 5]. The graphs in Figure 4 c) are composed of zero-dimensional vertices, one-dimensional edges and two-dimensional plaquettes. We apply measures, such as Minkowski functionals [15], to capture topological features of the graphs and their stabilities up to two dimensions and graph analysis measures like the diameter D_C and radius R_C to analyze the cluster structures of edge graphs [2]. The results of a selection of these topological measures are seen in Figure 4 c), for an extended list see Figure 5 in the appendix. Again most measures show a strong alignment or at least similar progression with mean accuracy of around [0.66 – 0.99], calculated via 5. This implies that our network is able to capture parts of the underlying topological structure with similar levels of stability, shown by the variance of the Euler-Characteristic χ_{full} in 4 c). To verify this we are currently analyzing higher temperature samples with more defects.

4 Conclusion and Outlook

In this work, we show that a generative U-net approach is able to generate physically realistic and topologically sound micro-magnetic vector configurations based on specific defect distributions. We have shown that our generated data is strongly aligned with simulated baseline data along most observables and shows consistent topology reconstruction evaluated using topological and graph-analytical measures. The latter indicating that an expansion to nematic models, with additional symmetries in the vector field is feasible.

In future work, we aim to enhance the networks strength to capture higher modes and analyze its performance at critical temperatures. Additionally, we will study the limits of our networks in terms of generalizing to larger lattice sizes and more complex defect structures as well as branching out to more generalized theories. These include the extension of our physical model to general Heisenberg models [3] with additional symmetries and higher order topological charges.

Acknowledgments and Disclosure of Funding

We acknowledge funding from the Emergent AI Center funded by the 'Carl-Zeiss-Stiftung', the TopDyn as research initiative of Rhineland Palatinate and funded by the Deutsche Forschungsgemeinschaft (DFG, German Research Foundation) - Project number 233630050 - TRR 146.

References

- [1] M. J. Beach, A. Golubeva, and R. G. Melko. Machine learning vortices at the kosterlitz-thouless transition. *Phys. Rev. B*, 97, 2018.
- [2] F. Buckley and F. Harary. *Distance in Graphs*. Addison-Wesley, 1990.
- [3] P. M. Chaikin and T. C. Lubensky. *Principles of Condensed Matter Physics*. Cambridge University Press, 1995.
- [4] F. Chazal and B. Michel. An introduction to topological data analysis: Fundamental and practical aspects for data scientists. *Front. Artif. Intell.*, 4:667963, Sept. 2021.
- [5] H. Edelsbrunner and J. Harer. Persistent homology—a survey. *Discrete & Computational Geometry - DCG*, 453, 01 2008.
- [6] M. Hasenbusch. The Two dimensional XY model at the transition temperature: A High precision Monte Carlo study. *J. Phys. A*, 38:5869–5884, 2005.

- [7] W. K. Hastings. Monte Carlo sampling methods using Markov chains and their applications. *Biometrika*, 57(1):97–109, 04 1970.
- [8] X. Hu, M. A. Nael, A. Wong, M. Lamm, and P. Fieguth. Runet: A robust unet architecture for image super-resolution. In *2019 IEEE/CVF Conference on Computer Vision and Pattern Recognition Workshops (CVPRW)*, pages 505–507, 2019.
- [9] G. Ishaan, A. Faruk, A. Martin, D. Vincent, and C. Aaron. Improved training of wasserstein gans. *arXiv:1704.00028*, 2017.
- [10] D. P. Kingma and J. Ba. Adam: A method for stochastic optimization, 2017.
- [11] D. Kuznedelev, V. Startsev, D. Shlenskii, and S. Kastryulin. Does diffusion beat gan in image super resolution?, 2024.
- [12] O. Lee, R. Msiska, M. A. Brems, M. Kläui, H. Kurebayashi, and K. Everschor-Sitte. Perspective on unconventional computing using magnetic skyrmions. *Applied Physics Letters*, 122(26):260501, 06 2023.
- [13] A. L. Maas. Rectifier nonlinearities improve neural network acoustic models. 2013.
- [14] A. Martin, C. Soumith, and B. Leon. Wasserstein gan. *arXiv:1701.07875v3*, 2017.
- [15] K. Mecke. *Additivity, Convexity, and Beyond: Applications of Minkowski Functionals in Statistical Physics*, volume 554, pages 111–184. 11 2008.
- [16] D. R. Nelson. Xvi. superfluidity and the two dimensional xy model. *Physics Reports*, 49(2):255–259, 1979.
- [17] A. Odena, V. Dumoulin, and C. Olah. Deconvolution and checkerboard artifacts. *Distill*, 2016.
- [18] S. Park, H. Yoon, D. Lee, J. Choi, H. Kwon, and C. Won. Topological magnetic structure generation using vae-gan hybrid model and discriminator-driven latent sampling. *Scientific Reports*, 13(1), Dec. 2023. Publisher Copyright: © 2023, The Author(s).
- [19] A. Paszke, S. Gross, F. Massa, A. Lerer, J. Bradbury, G. Chanan, T. Killeen, Z. Lin, N. Gimelshein, L. Antiga, A. Desmaison, A. Kopf, E. Yang, Z. DeVito, M. Raison, A. Tejani, S. Chilamkurthy, B. Steiner, L. Fang, J. Bai, and S. Chintala. Pytorch: An imperative style, high-performance deep learning library. In *Advances in Neural Information Processing Systems 32*, pages 8024–8035. Curran Associates, Inc., 2019.
- [20] C. Peng, T. Turiv, Y. Guo, Q.-H. Wei, and O. D. Lavrentovich. Command of active matter by topological defects and patterns. *Science*, 354(6314):882–885, 2016.
- [21] O. Ronneberger, P. Fischer, and T. Brox. U-net: Convolutional networks for biomedical image segmentation. In *Medical Image Computing and Computer-Assisted Intervention (MICCAI)*, volume 9351 of *LNCS*, pages 234–241. Springer, 2015. (available on arXiv:1505.04597 [cs.CV]).
- [22] N. Sale, J. Giansiracusa, and B. Lucini. Quantitative analysis of phase transitions in two-dimensional *xy* models using persistent homology. *Phys. Rev. E*, 105:024121, Feb 2022.
- [23] D. Ulyanov, A. Vedaldi, and V. Lempitsky. Instance normalization: The missing ingredient for fast stylization, 2017.
- [24] M. Walters, Q. Wei, and J. Z. Y. Chen. Machine learning topological defects of confined liquid crystals in two dimensions. *Phys. Rev. E*, 99:062701, Jun 2019.

Appendix

The accuracy values from chapter 3 are calculated in the following ways:

For the physical measures (Figure 4 a)-b) we use the coefficient of determination R^2 , calculated by:

$$R^2 = 1 - \frac{\sum(y_{real} - y_{pred})^2}{\sum(y_{real} - \bar{y}_{real})^2} \quad (4)$$

A value of one implies a perfect fit, while values lower than zero imply a fit worse than a mean predictor. For the topological measures (Figure 4 c) we opted for a different approach. We are interested in how often the true and predicted values are aligned, but not in the extent of possible errors. We therefore calculate the topological accuracy via:

$$Acc_{topo} = \frac{1}{n} \sum_{i=1}^n \llbracket |y_{pred} - y_{real}| < 0.05 \cdot \max(y_{real}) \rrbracket \quad (5)$$

This captures how often our generated data deviates less than 5% of the maximum value from the real data.

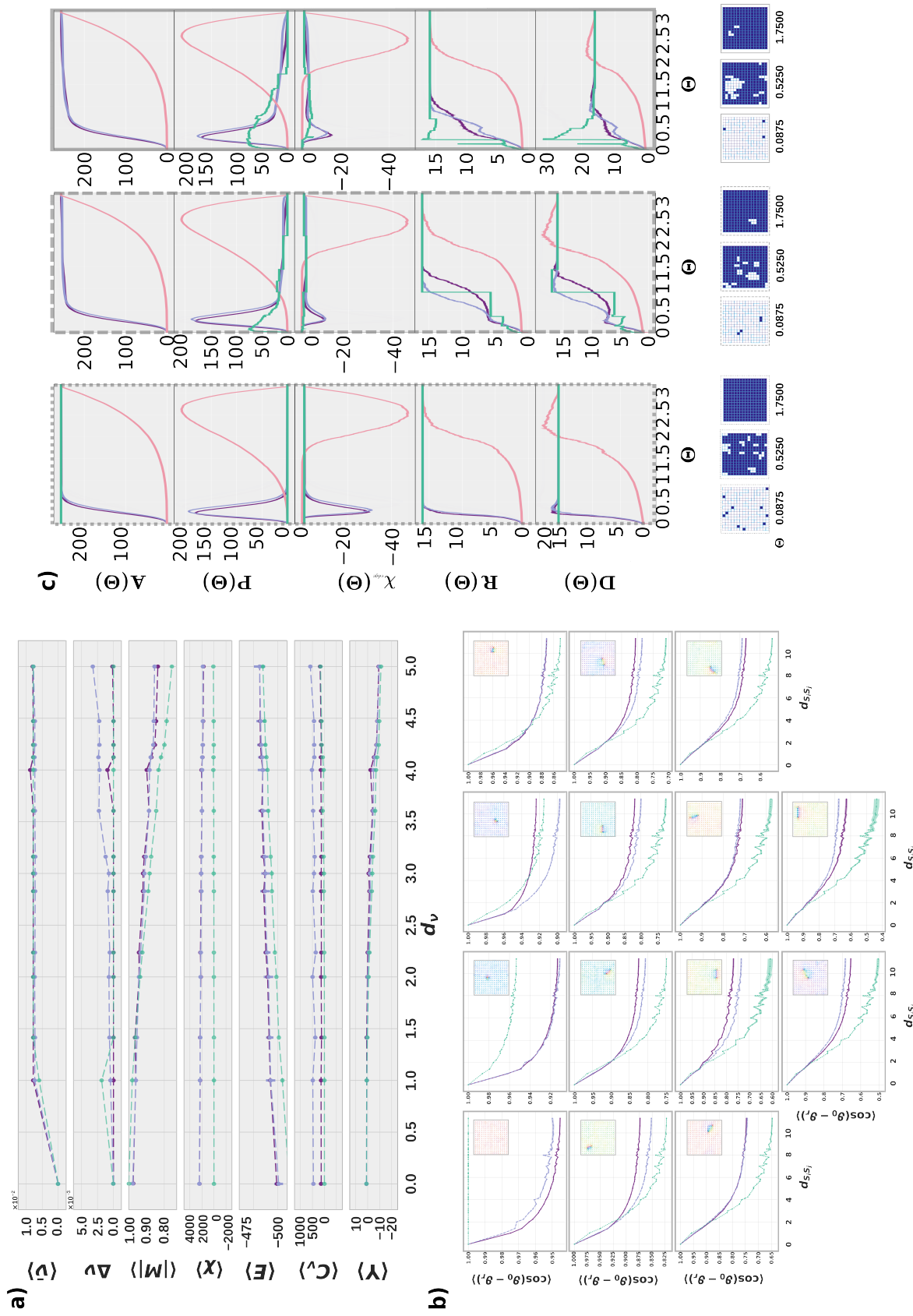


Figure 5: Comparison of measures based on the analysis of generated (light violet) with simulated (dark violet) magnetic vector fields in $T = 0$ (*light green*) and Gaussian distributed magnetic vector fields: a) Physical measures: [topological charge difference $\langle \nu \rangle$; magnetisation $\langle |M| \rangle$; energy $\langle E \rangle$; specific heat $\langle C_V \rangle$; helicity modulus $\langle \chi \rangle$; magnetic susceptibility $\langle \chi \rangle$; helicity $\langle Y \rangle$] depending on defect pair distance d_ν ; b) Global micro magnetic vector correlation function for $d_\nu = [0, 1, 1.41, 2, 2.24, 2.83, 3, 3.16, 3.61, 4.0, 4.12, 4.47, 5]$ [*from left to right, top to bottom*], with representative generated examples; c) Topological measures [area A ; perimeter P ; Edge-Euler-Characteristic χ ; edge radius R ; diameter D] for series of graph representations respectively for a set of 100 sampled micro-magnetic vector fields depending on filtration parameter Θ , with no defects $d_\nu = 0$. (*left*), close defects $d_\nu = 2$. (*middle*) and far defects $d_\nu \approx 4.14$ (*right*) with exemplary graph representations respectively to samples in b)